



Photocatalytic degradation of methylene blue over MIL-100(Fe)/GO composites: a performance and kinetic study

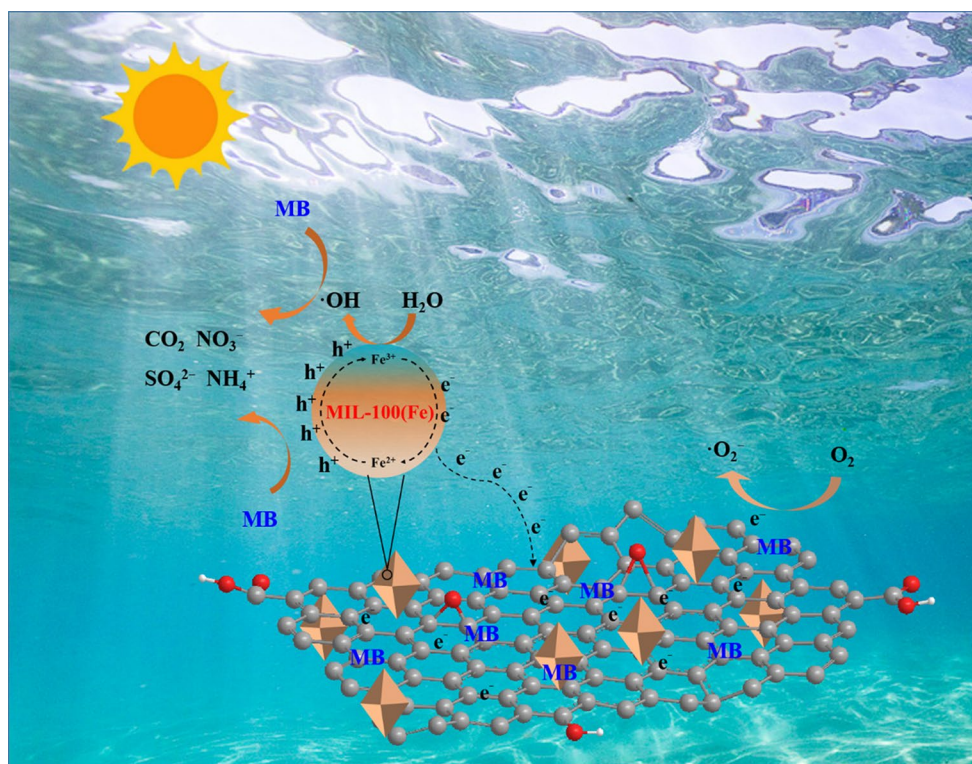
Yuxue Wei¹ · Zhiyuan Fu¹ · Yingzi Meng² · Chun Li² · Fu Yin¹ · Xue Wang¹ · Chenghua Zhang¹ · Lisheng Guo¹ and Song Sun¹

Received: 5 April 2023 / Revised: 5 September 2023 / Accepted: 11 March 2024
© The Author(s) 2024

Abstract

Adsorption coupled with photocatalytic degradation is proposed to fulfill the removal and thorough elimination of organic dyes. Herein, we report a facile hydrothermal synthesis of MIL-100(Fe)/GO photocatalysts. The adsorption and photocatalytic degradation process of methylene blue (MB) on MIL-100(Fe)/GO composites were systematically studied from performance and kinetic perspectives. A possible adsorption-photocatalytic degradation mechanism is proposed. The optimized 1M8G composite achieves 95% MB removal (60.8 mg/g) in 210 min and displays well recyclability over ten cycles. The obtained MB adsorption and degradation results are well fitted onto Langmuir isotherm and pseudo-second order kinetic model. This study shed light on the design of MOFs based composites for water treatment.

Graphical Abstract



Keywords Graphene oxide · Metal organic frameworks · Methylene blue · Adsorption · Photocatalytic degradation

Yuxue Wei and Zhiyuan Fu contributed equally to this work.

Extended author information available on the last page of the article

1 Introduction

With the rapid developments of chemical industry, the resulting substantial effluents have been discharged into environment, which bring serious disasters to humans (Zahra et al. 2020). It has been reported an ultimate water crisis will occur in the following decades, if measures are not taken to handle the massive loads of effluents with poisonous pollutants (Sol et al. 2020). Methylene blue (MB) is a prevalent organic dye in printing, cosmetics and leather tanning, which has low biodegradability (Ren et al. 2022). Efficiently removing MB from water is an important issue and has aroused extensive attention in academic field during the past few years. Variety of physicochemical techniques have been explored to eliminate organic dyes from waste liquid, such as precipitation (Sabbah et al. 2006), adsorption (Petit and Bandosz 2011), ion exchange (Horcajada et al. 2006), photocatalysis (Soltani et al. 2022) and electrochemical (Zhang et al. 2020). Among the above methods, adsorption has been an excellent unit operation to be widely applied in industrial production owing to its low cost, convenient operation and low sensitivity to toxicants. Nevertheless, re-desorption of pollutants is usually accompanied with adsorption treatment. Photocatalytic degradation (PCD) method is capable of complete removal of pollutants and intermediates, which requires the reaction system is optically transparent or has a certain degree of light transmission. Based on this prerequisite, PCD usually fails to treat dye effluents with high concentration. In this case, adsorption followed by photocatalysis is a promising route to fulfill pollutant removal in a wide range of concentration, which has attracted increasing attentions in both academic and industrial field (Du et al. 2022; Zhang et al. 2022). MB has been widely used as a model dye contaminant for assessing the adsorption and photocatalyst activity.

In progress to exploit superior dye removal performance, porous structured adsorbents like carbon-based material, zeolites, and metal-organic frameworks (MOFs) have been extensively studied (Xu et al. 2021; Tang et al. 2023). MOFs are a class of organic-inorganic hybrid materials formed by the ligand self-assembly of metal ions and organic ligands, which show extensive potential applications in catalysis, adsorption, gas storage and drug delivery (Horcajada et al. 2006). Nevertheless, MOFs-based materials display a variety of shortcomings, including poor stability, limited solar conversion efficiency and complicated separation and recycling processes during adsorption and photocatalytic degradation. Of note, although some MOFs are visible light responsive, the poor separation and migration of photo-induced charge carriers significantly restrict its application.

Doping, cocatalyst loading, surface modification and hybrid construction have been widely used to enhance the efficiency of MOFs-based photocatalysts by suppressing the recombination of charge carriers (Shuquan et al. 2015). Graphene oxide (GO) with two-dimensional layered structure have been utilized to construct hybrid photocatalysts, favoring the electron transfer and thus, inhibiting the recombination of charge carriers. Yang and co-workers have synthesized MIL-53(Fe)-graphene composites for selective oxidation of alcohols (Yang et al. 2016). GO/NH₂-MIL-125(Ti) has been fabricated and utilized for gaseous pollutants removal, which show high efficiency than bare NH₂-MIL-125(Ti) (Li et al. 2018). The introduction of GO into MOFs is believed to enhance its mechanical strength and electron-hole transfer. It is conceivable MOFs/GO composites serve as a promising candidate to mitigate the drawbacks reported for adsorbent and photocatalyst.

In virtue of facile synthesis, environment friendly and easy to scale up, MIL-100(Fe) is chosen to couple with GO to fulfill adsorption and photocatalytic degradation of MB. The performance of MIL-100(Fe)/GO composites in adsorption and adsorption-PCD process are systematically studied. Various structure and optoelectronic characterization techniques have been applied to systematically investigate the physicochemical properties of as-prepared composites. The adsorption isotherm and kinetic experiment are thoroughly studied for the adsorption and adsorption-PCD process.

2 Experimental section

2.1 Preparation of catalysts

9.2 g iron nitrate Fe(NO₃)₃·9H₂O, 3.2 g 1,3,5-benzenetricarboxylic acid H₃BTC, 106 mL distilled water and 1 mL nitric acid HNO₃ were mixed under 30 min stirring in a beaker, which were transferred into a Teflon-lined autoclave at 120°C for 24 h. After washed 3 h with hot water and ethanol, the obtained materials were filtered and dried at 120°C for 12 h, which named as MIL-100(Fe).

MIL-100(Fe)/GO composites were fabricated by a hydrothermal method similar to MIL-100(Fe). In a typical synthesis of 1M1G, 53 mL GO sel (10 mg/mL) were added dropwise into the aforementioned MIL-100(Fe) solution under mild stirring, which were further transferred into a Teflon-sealed autoclave at 120°C for 12 h. The subsequent filtration and wash procedures were analogous to MIL-100(Fe). Similarly, 212 mL, 424 mL and 848 mL GO sel were added. The resulting products were marked as 1M4G, 1M8G and 1M16G, respectively.

2.2 Characterizations

Bruker D8 diffractometer was applied to collect X-ray diffraction (XRD) pattern of as-prepared composites. Raman studies employed a Bruker-RFS27. Nicolet 6700 was utilized to determine the Fourier transform infrared spectroscopy (FTIR). Mettler-Toledo device was used for thermo gravimetric analysis (TGA) at a ramp rate of 10°C/min up to 900°C under argon flow. N₂ physisorption was conducted on ASAP-2020. Scanning electron microscopy (SEM) and Transmission electron microscopy (TEM) were performed on Regulus 8230 and FEI F200A. Hitachi U-4100 was applied to obtain UV-visible diffuse reflectance spectra (UV-vis DRS). Hitachi F-4500 was used to obtain photoluminescence spectra (PL). The transient photocurrent response was performed on CHI 760E electrochemical workplace. Na₂SO₄ (1 M) electrolyte solution and three-electrode system (glassy carbon electrode, platinum gauze electrode and Ag/AgCl electrode) were used under 300 W Xe lamp illumination (AM1.5). Auto Chem II 2920 was utilized to measure Ammonia-Temperature programmed desorption (NH₃-TPD). Thermo 250Xi was applied for X-ray photoelectron spectroscopy (XPS) measurements.

2.3 MB removal experiments

Adsorption and PCD experiments of MB were performed in a double glass reactor at room temperature by circulating cooling water. UV-3450 spectrophotometer was utilized to measure the MB concentration. For adsorption experiment, 0.1 L MB solution containing 0.1 g samples was stirred in dark at 700 rpm. For adsorption-PCD experiment, 0.1 L MB solution containing 0.1 g samples was stirred in dark for 30 min to reach adsorption-desorption equilibrium, and then exposed to simulated solar light using Xe lamp (300 W, AM 1.5). The average irradiation intensity of Xe lamp is 440 mW/cm².

3 Results and discussion

3.1 Characterization of as-prepared composites

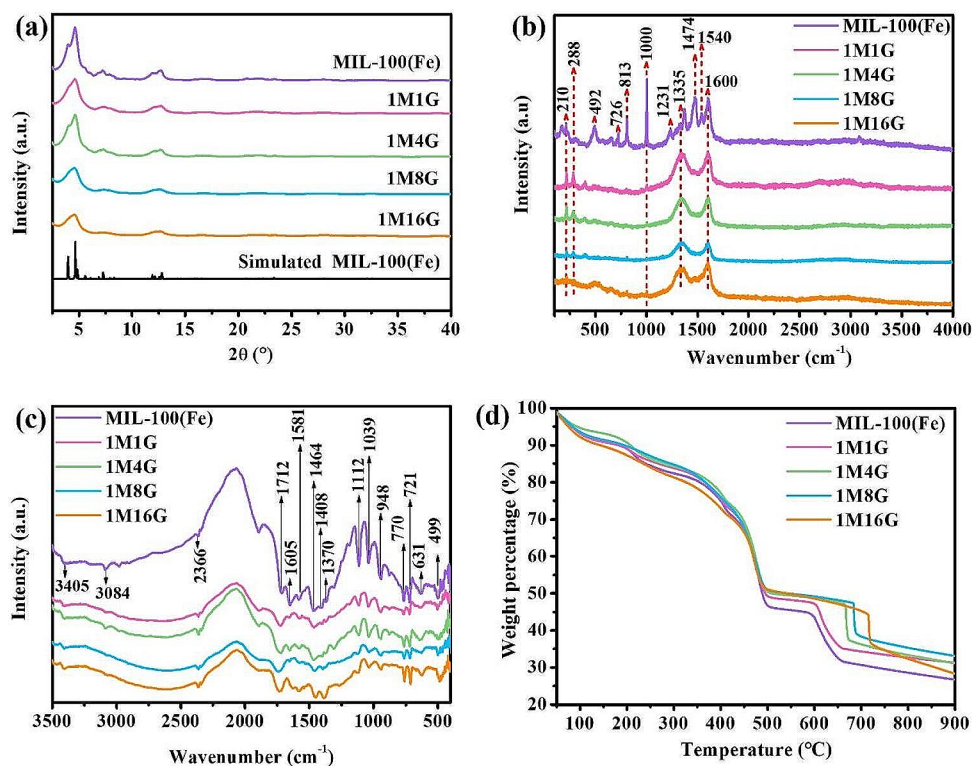
XRD patterns were recorded to determine the phase composition and crystallinity of as-prepared samples, as shown in Fig. 1a. The diffraction peaks of MIL-100(Fe) match well with the MIL-100(Fe) standard database (CCDC640536), demonstrating the MIL-100(Fe) has been successfully synthesized. The XRD, SEM, and TEM characterization of pristine GO are given in supporting information. A strong diffraction peak in XRD pattern at $2\theta = 15.5^\circ$ is attributed to the (110) crystal plane of GO (Figure S1). SEM and

TEM images indicate GO exhibit sheet morphology with certain wrinkles (Figure S2 and S3). The main XRD diffraction peaks from MIL-100(Fe) are preserved after GO incorporation, but with weak intensity and wide peak width. This phenomenon is more pronounced with further increment in GO incorporation, which is also reported by other groups (Petit and Bandoz 2011). It is conceivable the presence of GO induce certain distortion in the cubic symmetry structure of MIL-100(Fe) (Hafizovic et al. 2007), resulting in weak crystallinity. The GO induced poor crystallinity in MIL-100(Fe)/GO composites is believed to facilitate the charge carrier transfer, and thus enhance the photocatalytic performance. No distinct diffraction peaks derived from GO are detected, manifesting the high dispersion and exfoliation of GO in MIL-100(Fe)/GO composites. The iron loading of MIL-100(Fe), 1M1G, 1M4G, 1M8G and 1M16G are 13.0%, 13.6%, 13.9%, 13.7% and 14.2%, respectively.

To further verify the presence of GO, Raman spectra of MIL-100(Fe)/GO composites were collected. As given in Fig. 1b, two peaks around 1335 and 1600 cm⁻¹ are observed in MIL-100(Fe)/GO composites, labeled as D and G bands. D band reflects the structural disorder/defect of graphene, whereas G band represents the sp² hybridized carbon atoms (C=C stretching), hence confirming the presence of GO in composites (Li et al. 2018). Compared with MIL-100(Fe)/GO composites, the D and G bands in MIL-100(Fe) become sharp and narrow. This is owing to the vibration of carboxylate and C=C bond originated from the benzene ring in MIL-100(Fe). Besides, the bands at 210, 288, 492, 1474 and 1540 cm⁻¹ are characteristic of vibrational modes directly involving Fe(III) and Fe(II) species in MIL-100(Fe) (Petit and Bandoz 2011). The peak at 813 cm⁻¹ can be attributed to the -COO- functional group bound to benzene ring, whereas the in-plane vibrations of H₃BTC are demonstrated by the peaks located at 726, 1000 and 1231 cm⁻¹ (Petit and Bandoz 2011). Interestingly, partial Raman bands derived from MIL-100(Fe) tend to weak and even disappear with the increment of GO incorporation, which can be attributed to the MIL-100(Fe) is sheltered by GO. This phenomenon implies the MIL-100(Fe) nanoparticles are well dispersed on GO layers. The Raman results also demonstrate that GO and Fe-O coordination structure are existed in MIL-100(Fe)/GO composites.

To elucidate the structure and functional groups of as-prepared samples, FTIR spectra were obtained (Fig. 1c). The as-prepared samples exhibit similar structural vibrations, since they are consisted of trivalent metal centers and carboxylate bridging ligands. The bands located at 499 cm⁻¹ and in the range of 631–770 cm⁻¹ are ascribed to Fe-O and Fe-OH stretching modes of MIL-100(Fe) (Hailin et al. 2019), indicating the iron metal interact with the oxygen atom from carboxyl group in H₃BTC. The bands appeared

Fig. 1 **a** XRD patterns **b** Raman spectra **c** FTIR spectra and **d** TGA profile of the as-prepared composites



at 948, 1039, 1112, 1370, 1408, 1464, 1581, and 1605 cm^{-1} originate from the carboxylate groups vibrations, which are in agreement with the literatures (Aslam et al. 2017). The presence of above-mentioned characteristic bands provides clear evidence of the successful fabrication of MIL-100(Fe). A shoulder at 1712 cm^{-1} indicates a small portion of carboxylate groups are protonated. The troughs at 2000–3500 cm^{-1} stem from the stretching vibrations of water molecules. After GO incorporation, the characteristic bands of MIL-100(Fe) are preserved but with weak intensity and slight shift. MIL-100(Fe) and GO have been successfully composited, which are in agreement with the XRD and Raman results.

To further verify the successful fabrication of MIL-100(Fe)/GO as well as thermal stability, TGA plots of as-prepared composites are shown in Fig. 1d. The composites display good thermal stability up to about 600°C. A certain weight loss (50% weight loss) appears below 600°C, which is assigned to the desorption of water and solvent molecules inside MIL-100(Fe) frameworks (Monika et al. 2018). The water molecules derived from hydrothermal synthesis induce more ligand defect sites in MOFs. A sharp weight loss of 20% is found in the temperature range of 600–800°C, manifesting the collapse of MIL-100(Fe) structure owing the decomposition of H_3BTC linker. The temperature of framework collapse in different samples increases with increasing GO content, indicating the combination of GO with MOFs effectively improve the thermal stability of

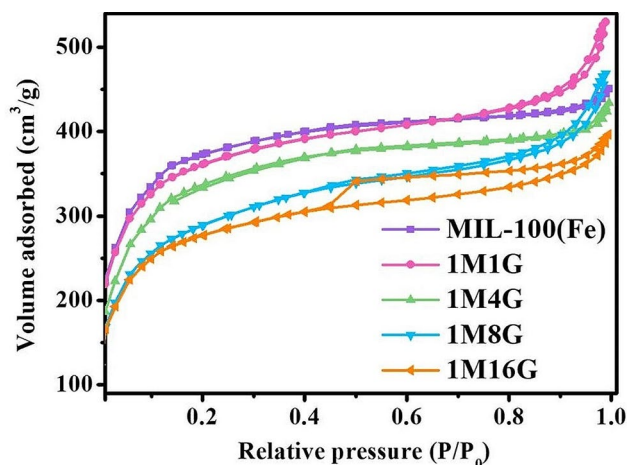


Fig. 2 N_2 adsorption-desorption isotherms (at 77 K) of MIL-100(Fe) and MIL-100(Fe)/GO composites

composites. It is conceivable the MIL-100(Fe) and GO are intimately integrated.

The N_2 adsorption-desorption isotherms, BET surface area and pore characteristics of as-prepared composites are given in Fig. 2 and Table 1. The MIL-100(Fe) and 1M4G show IUPAC type I adsorption curves, suggesting the presence of abundant micropores. 1M1G and 1M8G show type IV adsorption curves in the high P/P_0 region, which represents the existence of meso-/macropores. The hysteresis loop tend to be obvious with the increase of GO incorporation. The 1M16G presents a type IV isotherm with an

apparent hysteresis loop, which is derived from the capillary condensation occurred in mesoporous structure. Look carefully at the curves, a rapid upstroke of N_2 adsorption at low relative pressure ($P/P_0 < 0.05$) is presented, which is associated with the microporous structure. These isotherms indicate the as-prepared composites display hierarchical pore structure, which is advantageous for their adsorption capacity and subsequent photocatalytic activity.

As given in Table 1, MIL-100(Fe) shows superior textural properties (specific surface area of $1316 \text{ m}^2/\text{g}$, total pore volume of $0.63 \text{ cm}^3/\text{g}$, average pore size of 33.4 nm). With the increment of GO incorporation, the specific surface area and pore volume of samples gradually decrease, which are related to GO may block some micropores in MIL-100(Fe) (Li et al. 2018). The 1M8G presents a specific surface area of $1031 \text{ m}^2/\text{g}$, total pore volume of $0.53 \text{ cm}^3/\text{g}$, and average pore size of 42.3 nm . It is found the pore structure of adsorbent determines the type and adsorption capacity of organic pollutants. Importantly, the pore sizes of as-prepared composites should be in accordance with the targeted molecule (Jiang et al. 2021). In the case of 1M8G, a

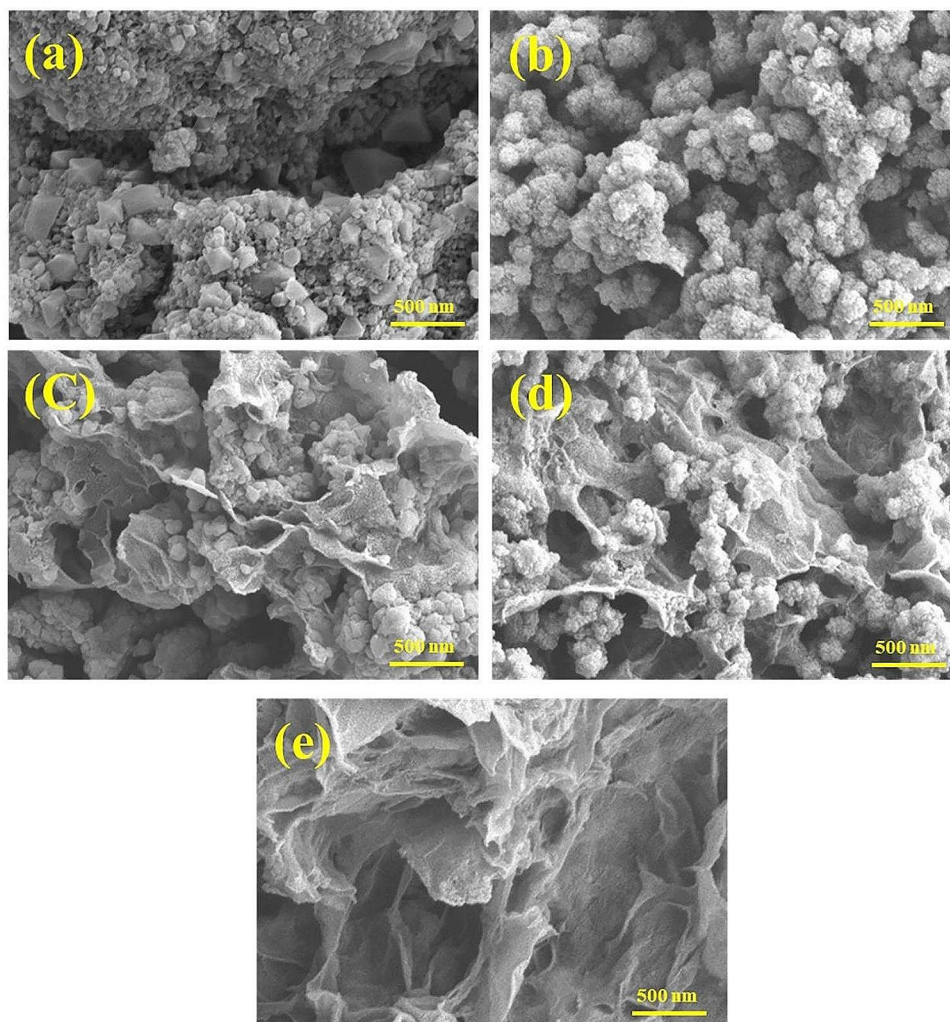
Table 1 Textural properties of as-prepared samples

Catalyst	S_{BET} (m^2/g)	S_{ext} (m^2/g)	Average pore size (nm)	Total pore volume (cm^3/g)
MIL-100(Fe)	1316	277	33.4	0.63
1M1G	1274	321	46.1	0.61
1M4G	1207	336	33.8	0.59
1M8G	1031	406	42.3	0.53
1M16G	982	296	37.8	0.53

high external specific surface area is achieved, which is key to enhance the adsorption ability and photocatalytic activity. It is believed the high surface area and porous structure of MIL-100(Fe)/GO composites allow easy entry of reactants.

As seen in Fig. 3a, MIL-100(Fe) present a well-defined octahedral morphology with certain amorphous structure. After GO incorporation, the MIL-100(Fe) nanoparticles tend to attach on GO sheet layer with uniform dispersion, which exhibit a rough surface and smaller particle size. The small crystalline size of MIL-100(Fe)/GO is also confirmed by the weak and broad diffraction peaks in XRD

Fig. 3 SEM images of **a** MIL-100(Fe), **b** 1M1G, **c** 1M4G, **d** 1M8G and **e** 1M16G



patterns. This is due to GO with abundant oxygen-containing groups can interact with the central metal ion Fe(III) in MIL-100(Fe), affecting the formation and growth of crystal nucleus. Further increasing GO content leads to the emergence of more GO sheet in MIL-100(Fe)/GO composites. TEM images of 1M8G are given in Figure S4, which illustrate the MIL-100(Fe) are well dispersed on GO with close vicinity.

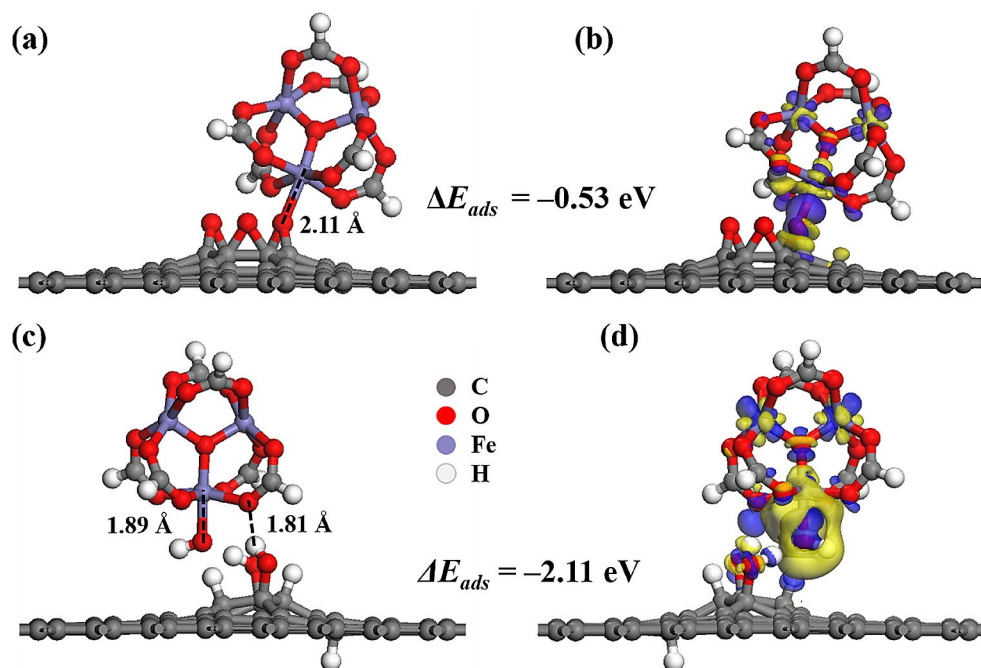
To understand the specific interaction between MIL-100(Fe) and GO at the molecular level, we have conducted the density functional theory (DFT) calculation. All calculations were performed within DFT framework by CASTEP code. Representative clusters of GO with hydroxyl and epoxy functional groups are denoted as GO-OH and GO-O, respectively. The optimized structure of MIL-100(Fe) and GO are shown in Figure S5. The binding energy between GO-O and MIL-100(Fe) is -0.53 eV, while that of GO-OH and MIL-100(Fe) is -2.11 eV (Fig. 4). It has been widely acknowledged the adsorption energy between -0.1 eV and -1 eV is physical adsorption, and that between -0.5 eV and -10 eV is chemical adsorption (Zhou et al. 2012; Dong et al. 2017). Therefore, it is reasonable the main interaction between GO and MIL-100(Fe) is chemical adsorption. Meanwhile, it can be seen from the bonding and electron transfer that the interaction between MIL-100(Fe) and GO can be attributed to chemical adsorption.

Based on the results discussed above, it is believed the intimate binding between GO and MIL-100(Fe) can not only enhance mechanical strength and stability of as-prepared composites, but also facilitate the transportation of photoinduced electrons and holes (Liu et al. 2018).

UV-vis DRS was used to analyze the optical characteristics of as-prepared samples. As given in Fig. 5a, MIL-100(Fe) and MIL-100(Fe)/GO composites show strong adsorption in ultraviolet and visible light range between 200 and 800 nm. The adsorption band in the region of 200–800 nm probably originates from the d-d spin-allowed transition of central Fe(III) ions, in accordance with previous reports (Liu et al. 2018). The adsorption edges at around 380 nm correspond to the adsorption of MIL-100(Fe) in UV range, which is related to the excitation of Fe-O clusters (Aslam et al. 2017). The efficient adsorption in ultraviolet and visible light confirms the samples are highly photosensitive. The addition of GO give rise to an increased light adsorption intensity in visible light region, which is further confirmed by PL and transient photocurrent response results. Based on the adsorption spectra, plotting $(\alpha h\nu)^{1/2}$ to $h\nu$ and then extrapolating the adsorption edge onto energy axis can give the band gap energy (E_g) of samples (Figure S6). The E_g of MIL-100(Fe), 1M1G, 1M4G, 1M8G and 1M16G are 2.94, 2.91, 2.58, 2.35 and 2.61 eV, respectively. The smallest E_g of 1M8G suggests higher probability of generating charge carriers and potentially higher photocatalytic activity.

Photoluminescence (PL) spectra of the samples were applied to investigate the photo-generated carriers recombination probability. Under the excitation wavelength of 560 nm at room temperature, as shown in Fig. 5b, the main emission peak of samples appears at 613 nm, which is attributed to the H₃BTC in MIL-100(Fe) structure (Ou et al. 2020). The PL intensity of samples followed the order: MIL-100(Fe) > 1M1G > 1M4G > 1M16G > 1M8G. The lower PL intensity in 1M8G composites manifests the longer lifetime

Fig. 4 Structure and electron density difference between **a, b** GO-O, **c, d** GO-OH and MIL(100)-Fe (blue and yellow areas indicate the loss and accumulation of electrons, respectively)



of photogenerated carriers, and thus higher photocatalytic activity is achieved. It is conceivable the intimate interfacial contact between MIL-100(Fe) and GO favors the separation and migration of photoinduced carriers, which can provide sufficient charge transfer and trapping channels (Yang et al. 2016). Besides, GO can serve as an acceptor for charge carriers (Petit and Bandosz 2011). The facilitated separation of long-lived carriers renders the MIL-100(Fe)/GO composites efficient for photocatalytic applications.

Figure 5c reveals the transient photocurrent response of as-prepared composites. The photocurrents display a regular rise and fall along with light switching, corresponding to the holes accumulation and recombination at the semiconductor-liquid junction (Li et al. 2015). It is evident the photocurrent intensity of MIL-100(Fe) is lower than that of MIL-100(Fe)/GO composites, suggesting the composites have higher charge carrier separation and migration efficiency, which can be ascribed to the synergistic effect of MIL-100(Fe) and GO. Specially, GO serves as an electron acceptor to facilitate carrier separation and transfer, which is in line with the conclusion drawn by PL analysis.

NH₃-TPD experiment has been performed to examine the surface acidic sites distribution. As shown in Fig. 5d, the samples exhibit three main NH₃ desorption peaks, which are caused by physical and chemical adsorption. The temperature required for NH₃ desorption directly correlates to the acid strength of samples. The amounts of NH₃ desorbed above 400°C reflects strong acidic sites, whereas the amount

of NH₃ desorbed in 250–400°C represents medium acidic sites and the amount of NH₃ desorbed below 250°C represents weak acidic sites (Zhu et al. 2016). Based on the location and area of desorption peaks in Fig. 5d, it can be concluded MIL-100(Fe) has a larger quantity of acid sites and stronger acid sites compared with others. The NH₃-TPD results also demonstrate the inherently strong adsorption properties of MIL-100(Fe). However, GO incorporation partially reduce the number of acidic sites, probably due to GO overlap the acid sites on MIL-100(Fe), corresponding to the decrement of specific surface area.

Figure 6 shows the XPS spectra of 1M8G. As shown in Fig. 6a, 1M8G exhibits various peaks at 726.07 eV, 532.66 eV, and 284.33 eV, corresponding to Fe 2p, O 1s, and C 1s. Fe 2p spectrum is fitted into two well-defined Fe 2p_{3/2} and Fe 2p_{1/2} peaks in Fig. 6b at 712.81 eV and 725.75 eV, with the separation (2p_{1/2}–2p_{3/2}) of 12.94 eV, which is characteristic of Fe-O clusters in MIL-100(Fe) (Li et al. 2018). The satellite peak at 717.70 eV is originated from Fe(III) (Ahmad et al. 2019). Moreover, the peak at 711.29 eV is attributed to Fe(II) (Ahmad et al. 2019). Figure 6c shows the C 1s spectra of 1M8G. The peaks at 284.80, 286.49 and 288.80 eV are assigned to C-C/C=C, C-O and O-C=O, respectively. As can be seen from the O 1s spectra of 1M8G in Fig. 6d, two well-defined peaks located at 533.80 eV and 531.86 eV are attributed to Fe-O and C-O/C=O (Tian et al. 2019). Based on XPS results, the successful integration of MIL-100(Fe) and GO are validated. The existence of Fe-O

Fig. 5 **a** UV-Vis **b** PL spectra **c** Transient photocurrent response in sodium sulphate electrolyte (pH = 7.0, 1 M) under Xe lamp illumination (AM1.5), and **d** NH₃-TPD patterns of the MIL-100(Fe) and MIL-100(Fe)/GO composites

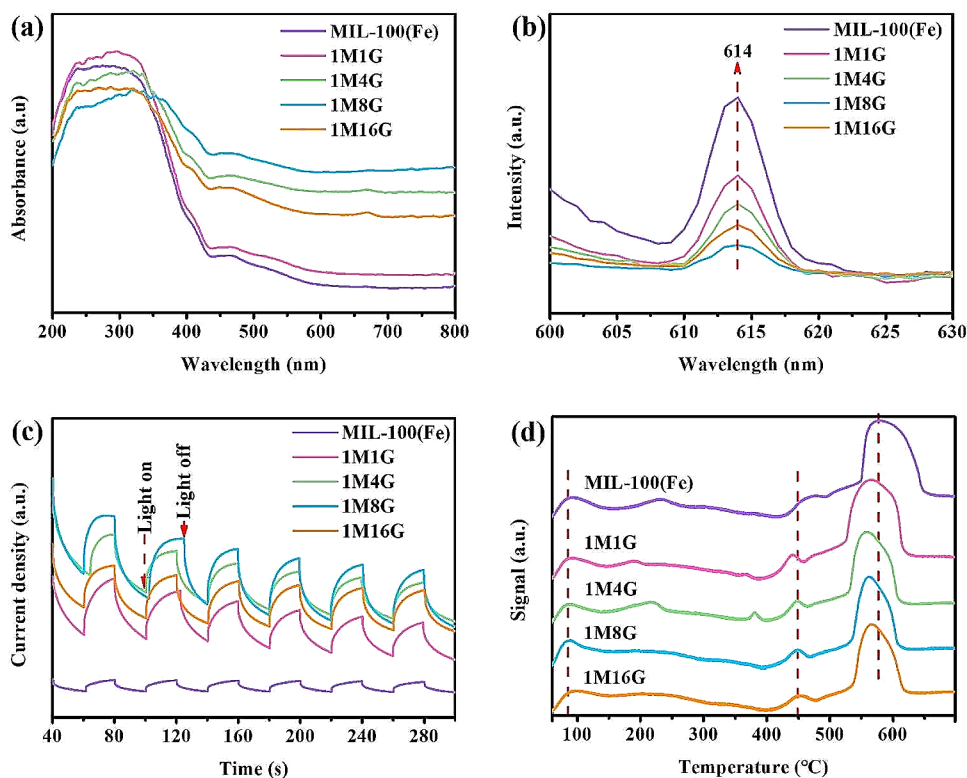
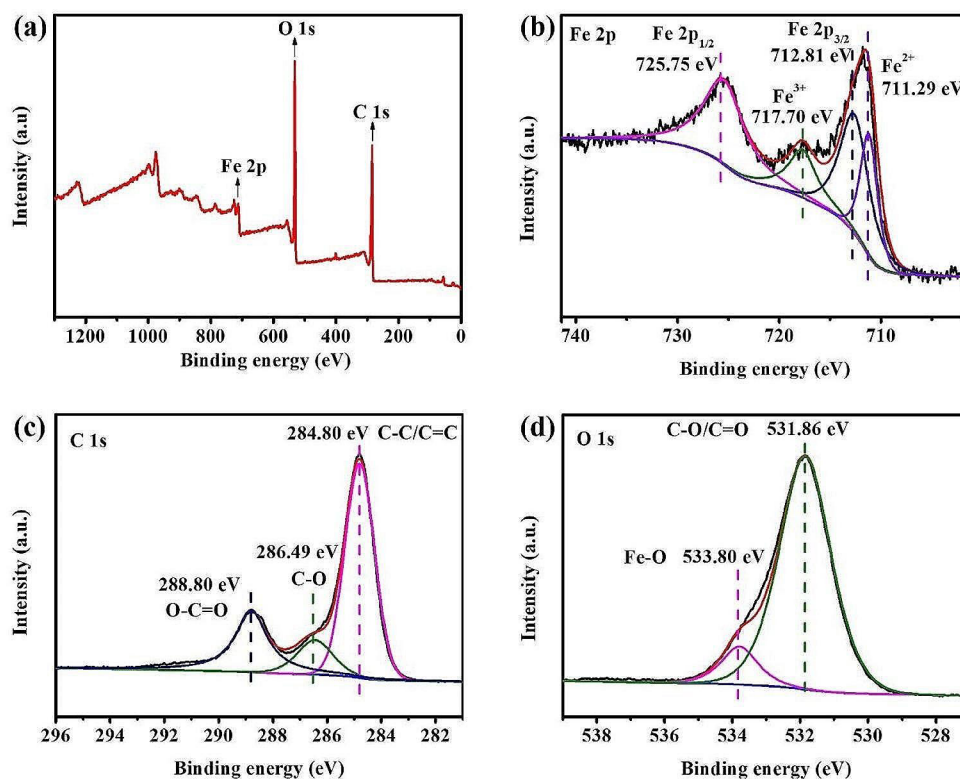


Fig. 6 **a** Survey, **b** Fe 2p, **c** C 1s, and **d** O 1s spectra of 1M8G



clusters within MOF structure is illustrated, agreeing well with Raman and FTIR results.

3.2 Performance study

The effective capture of organic pollutants is a significant prerequisite for photocatalytic degradation. As shown in Fig. 7a, the adsorption curve of as-prepared samples demonstrate a rapid increasing stage before 5 min with a removal of MB of 50%–70%, and then a slow adsorption stage is observed within 5–30 min. The initial rapid adsorption of MB is due to the availability of sufficient vacant adsorption sites, which enable the dye molecules to interact readily at the adsorbent surface. Compared with MIL-100(Fe), GO incorporation enhances the adsorption ability for MB. GO content has a significant effect on the adsorption performance. As the GO content increases, the MB removal efficiency increase and reach a peak value with 1M8G. Approximate 85% MB is adsorbed in the 1M8G composites at 30 min. According to XRD results, GO incorporation reduces the crystallinity of MIL-100(Fe) to some extent. The weak crystallinity of MIL-100(Fe)/GO composite is conducive to the enhancement of adsorption capacity. Meanwhile, the increment of GO dosage is equivalent to an increase in the number of functional groups (epoxy, hydroxyl, and carboxyl groups) involved in adsorption. The oxygen-containing functional groups in GO have been considered as adsorption sites

for MB (Yang et al. 2016). Furthermore, the incorporation of GO into MOFs makes the MIL-100(Fe) well dispersed, inducing more active sites for MB adsorption, as confirmed by SEM. Further increasing GO content, the removal capacity of MB declines to 68%. It is believed the degree of adsorption rely on the porosity and surface area of adsorbent. Excessive GO can cover the MIL-100(Fe) surface, leading to a decrement of surface area and pore volume, and thus, affecting the adsorption and mass transfer capacities of MIL-100(Fe)/GO composites. Moreover, the adsorption capacity strongly rely on the micropores of MOFs, as previously reported by Hu et al. (Hu et al. 2015).

In view of the outstanding adsorption performance of 1M8G, adsorption tests (marked as dark) with different MB concentration (100–400 $\mu\text{mol/L}$) have been conducted and the outcomes are displayed in Fig. 7b. The adsorption capacity of 1M8G on MB slightly increases and gradually flattens out with the prolonged adsorption time. When the adsorption time reaches to 210 min, the equilibrium adsorption is achieved regardless of initial MB concentration of 100, 200 or 400 $\mu\text{mol/L}$. When the initial concentration of MB increases from 100 $\mu\text{mol/L}$ to 200 $\mu\text{mol/L}$ and 400 $\mu\text{mol/L}$, the adsorption efficiency of 1M8G decreases significantly from 98 to 81% and 45% respectively. This can be explained by the lack of active sites in composites in comparison with the excess MB. Meanwhile, the adsorption saturation is proportional to the initial concentration of MB,

which also responsible for the low adsorption efficiency at high initial concentrations.

Taking the low adsorption efficiency of 1M8G under high MB concentration into account, photocatalytic degradation is applied to achieve highly efficient removal of MB. Figure 7b shows the adsorption-PCD performance (marked as light). After 30 min adsorption, stimulated solar light irradiation was introduced into the system. As can be seen, high removal of MB occur with the reaction time prolongs. For low concentration MB aqueous solution (100 $\mu\text{mol/L}$), the light irradiation slightly affect the MB removal, which has significant influence on the MB removal under high MB concentrations. Notably, for 1M8G composite, which display weak adsorption ability under high concentration MB, 95% removal of MB (200 $\mu\text{mol/L}$) is achieved in 210 min by the combination of adsorption and photocatalysis. The 1M8G sample achieves 60.8 mg/g MB removal efficiency under sunlight, which is higher than the previous studies, as shown in Table S1. It can be seen most studies of MB removal involves the utilization of H_2O_2 , UV light and low initial MB concentration. In this sense, the developed MOFs/GO composites can act as a potential material in the application for organic dye removal, especially in high concentration. Even if the initial MB concentration is as high as 400 $\mu\text{mol/L}$, the adsorption-PCD method arouse a ca. 20% enhancement of MB removal compared with adsorption route, which shows ca. 60% MB removal efficiency. For adsorption-PCD method, the MB removal efficiency also decrease with the increment of initial MB concentration. This can be ascribed to the excess dye molecules around active sites inhibit the penetration of light to catalyst surface, leading to a decrement of photogenerated charge carriers.

The adsorption-PCD tests of methyl orange, rhodamine B, and congo red with an initial concentration of 200 $\mu\text{mol/L}$ on 1M8G have been conducted. As given in Figure S7, congo red has the highest removal efficiency of 100% within 210 min, while methyl orange and rhodamine B show removal efficiency of 55.7% and 36.6%, respectively. It is obvious the as-prepared 1M8G composites act differently in adsorption-PCD process of these organic dyes. This

can be attributed to their different structures, sizes and electric charges that led to different degree of adsorption and degradation on the surface of catalyst (Ghosh et al. 2020).

Regeneration study is crucial for adsorbent and photocatalyst considering the cost issue. The recyclability and stability of 1M8G were tested by performing ten cycles. After each cycle, the sample was recovered by centrifugation and washed with 50 mL N,N-dimethylformamide (DMF) to fully remove the dye. Subsequently, the sample was solvent-exchanged with water to remove the DMF from the structure and dried in an oven at 80°C for 12 h for next cycle. During the regeneration process, the weight of sample remains basically unchanged. The sample recovery ratio obtained after each cycle is above 95%. Figure 8 shows the degradation efficiency maintain >90% within 210 min in every repetition. After ten cycles, the removal efficiency of MB slightly reduce to 90%. The slight reduction in the MB removal after each cycle can be ascribed to the accessibility of light is impeded and reduced porosity of catalyst.

In contrast, the degradation efficiency of MIL-100(Fe) significantly decreases to 23% after ten cycles (Figure S8), which can be attributed to the aggregation of NPs and weak water stability, as confirmed by the SEM (Figure S9) and static water contact angle (CA) results (Figure S10). Based on the results discussed above, it is believed the intimate binding between GO and MIL-100(Fe) can not only enhance mechanical strength and stability of as-prepared composites, but also facilitate the transportation of photoinduced electrons and holes. Of note, the presented regeneration methods of MOFs/GO adsorbents are still rigorous and time-consuming. Researches are needed to identify cost-effective and better physico-chemical methods for regenerating the spent adsorbent.

3.3 Adsorption isotherms

For heterogeneous catalysis, adsorption is the prerequisite to improve the catalytic performance. The adsorption and desorption between reactants, intermediates and photocatalyst surface is a key factor affecting activity and selectivity. Hence, the cognition of adsorption configuration play

Fig. 7 **a** Adsorption test of as-prepared samples at 100 $\mu\text{mol/L}$ MB and **b** adsorption and adsorption-PCD test of 1M8G at different MB concentration

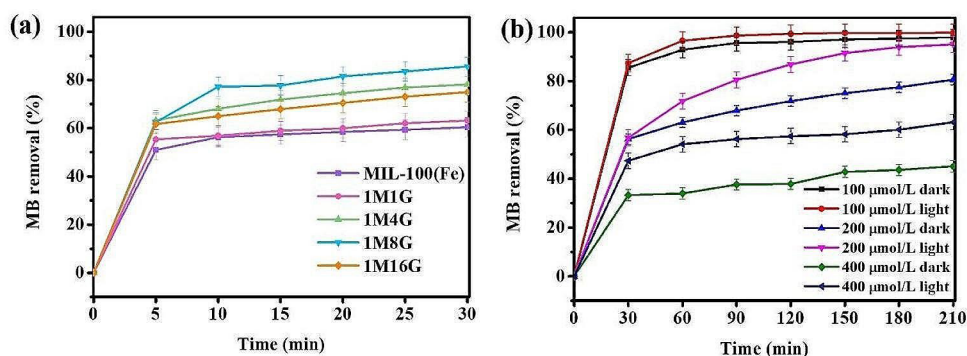


Fig. 8 Adsorption-PCD recycle test of 1M8G at 200 $\mu\text{mol/L}$ MB

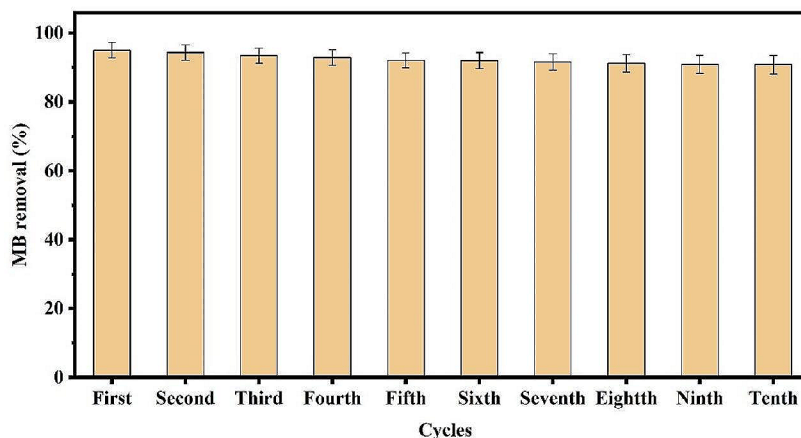


Fig. 9 **a** Langmuir isotherm model, **b** Freundlich isotherm models fitting results of MB adsorption

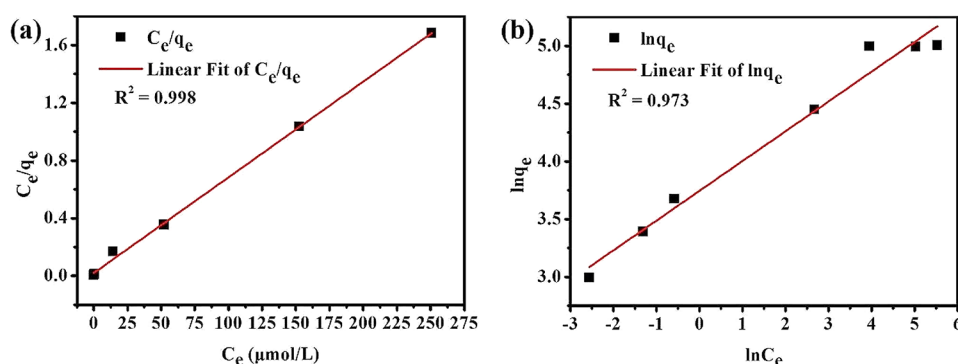


Table 2 Adsorption isotherm parameters for MB adsorption on 1M8G

Isotherm model	Parameters	1M8G
Langmuir	q_m ($\mu\text{mol/g}$)	151.0
	K_L ($\text{L}/\mu\text{mol}$)	0.3
	R^2	0.998
Freundlich	n	3.9
	K_F	42.3
	R^2	0.973

significant roles in illuminating the catalytic mechanism. Langmuir and Freundlich models were used to investigate the MB adsorption process over 1M8G. The isotherm fitting curves of adsorption process and relevant kinetic parameters are given in Fig. 9 and Table 2. Monolayer adsorption is characteristic of Langmuir model, while Freundlich model represents multilayer adsorption. Langmuir adsorption isotherm assumes the adsorption occurs at a finite number of definite localized sites with no interaction. Freundlich adsorption isotherm suggests the adsorbent surface has unequal available sites with different adsorption energy; the adsorption energy decreases exponentially during adsorption process. The Freundlich isotherm considers the surface heterogeneity. Correlation coefficient (R^2) is used to evaluate the applicability of the adsorption model. The following are the isotherm model formulas (Nehra et al. 2019).

Langmuir model:

$$\frac{C_e}{q_e} = \frac{C_e K_L + 1}{q_m K_L} \quad (1)$$

Freundlich model:

$$\ln q_e = \ln(K_F) + \frac{1}{n} \ln C_e \quad (2)$$

C_e ($\mu\text{mol/L}$) denotes the equilibrium MB concentration, q_e ($\mu\text{mol/g}$) denotes the equilibrium adsorption capacity, q_m ($\mu\text{mol/g}$) denotes the maximum adsorption capacity, K_L and K_F denote the Langmuir model constant (L/mg) and Freundlich model constant.

The fitting curves show Langmuir isotherm model is appropriate for MB adsorption over 1M8G with a correlation coefficients value of 0.998. Light transmittance has been reported as a crucial factor influencing photocatalytic activity (Emam et al. 2020). The monolayer adsorption of MB on 1M8G, which is characteristic of Langmuir isotherm model, is advantageous for light transmittance (Koo et al. 2004). Moreover, it is proposed chemisorption plays a dominant role in monolayer adsorption, which endow the

adsorbate strongly bind to the surface of adsorbent via electrostatic and hydrogen bonds. The intense binding between MB and 1M8G reduces the possibility of desorption, which is detrimental for the adsorption treatment. In contrast, multilayer adsorption presents a physical binding, related to less intense interactions such as hydrogen bonds and van der Waals forces (Koo et al. 2004). Overall, it is reasonable the monolayer coverage of MB on 1M8G favors the adsorption and subsequent photocatalytic degradation of adsorbed MB.

Figure S11 shows the correlation between equilibrium adsorption capacity and initial MB concentration. It can be clearly seen the adsorption capacity is linearly and positively correlated with MB concentration in low concentration region, which can be ascribed to the driving force associated with concentration. A further increase in concentration causes a slow increase in adsorption capacity. This is because a finite number of adsorptive sites have been occupied by MB molecules.

3.4 Kinetic study

The adsorption mechanism and rate-determining step can be analyzed by kinetic models. To assess the MB degradation response kinetics, pseudo-first and pseudo-second order kinetic models have been utilized to analyze the obtained data. Pseudo-first and pseudo-second order are two commonly used kinetic models. The former presumes adsorption rate rises in proportion to the number of unoccupied adsorption sites, while the latter presumes adsorption is a chemical process. The following are the kinetic calculation formulas (Nehra et al. 2019):

Pseudo-first order model:

$$\log(q_e - q_t) = \log(q_e) - \frac{k_1}{2.303}t \quad (3)$$

Pseudo-second order model:

$$\frac{t}{q_t} = \frac{1}{k_2 q_e^2} + \frac{t}{q_e} \quad (4)$$

k_1 (min^{-1}) and k_2 ($\text{g} \cdot \mu\text{mol}^{-1} \cdot \text{min}^{-1}$) denote pseudo-first and pseudo-second order kinetic rate constants; q_t and q_e denotes the capacity of adsorbed MB at time t and equilibrium, respectively.

The kinetic results and relative parameters for adsorption and adsorption-PCD processes are given in Fig. 10 and Table S2. Based on the fitting results, pseudo-second order model is suitable for the description of MB adsorption and adsorption-PCD process with higher correlation coefficient R^2 , in comparison with pseudo-first order model. The calculated q_e based on pseudo-second order model is close to

the experimental q_e . Hence, it is deduced MB adsorption adopt pseudo-second order kinetics model, indicating the adsorption rate is dominated by chemisorption and chemisorption is the rate-determining step. This result is in line with the adsorption isotherm study. According to FTIR results (Figure S12), the peaks at 880, 1331 and 1532 cm^{-1} after adsorption represent the vibration of MB dye, demonstrating the chemisorption of MB over 1M8G (Aslam et al. 2017). Similar to adsorption process, the degradation of MB under adsorption-PCD conditions follows pseudo-second order kinetic model, indicating the adsorption rate is dominated by chemical adsorption that involves electron sharing/transfer between adsorbent and adsorbate. Chemical adsorption minimises the potential for desorption and achieves efficient removal of pollutants. Importantly, with the increment of MB concentration, the light irradiation exhibit remarkable influence on MB removal.

However, owing to the finite sites for reaction, the MB removal efficiency gradually decreases and flattens out, which is confirmed by the experimental results. As shown in Figure S13, a long time adsorption-PCD experiment of 1M8G at 200 $\mu\text{mol/L}$ MB have been conducted. The MB removal efficiency of 1M8G on MB significantly increases within 150 min and gradually flattens out with the prolonged reaction time. A plateau is reached after 210 min reaction. Similar phenomena have been observed in the dye adsorption on adsorbents (Hameed et al. 2007).

3.5 Proposed mechanism

Adsorption isotherm and kinetic study suggest the adsorption of MB dye over MIL-100(Fe)/GO composite obeys Langmuir isotherm model and the pseudo-second order model, indicating chemical adsorption plays a dominant role. As shown in XPS, diverse oxygen-containing functional groups are existed in the MIL-100(Fe)/GO, arousing negative charge in neutral environment. During adsorption process, the cationic dye MB can interact with the negatively charged functional groups in the composites via electrostatic interaction. The aromatic ring structures existed in GO and MIL-100(Fe) favors MB adsorption via π - π interactions and hydrogen bonds. Also, the nitrogen atoms in MB structure are expected to form hydrogen bonds with -OH groups in MIL-100(Fe)/GO (Vargas et al. 2011). Therefore, a possible adsorption mechanism of MB dye on MIL-100(Fe)/GO composites is proposed including π - π stacking, electrostatic interactions and hydrogen bonds.

The basic reaction mechanism of photocatalytic degradation process involves the excitation of electrons and holes induced by light irradiation in Fe(II)/(III)-O clusters of MIL100(Fe)/GO composites. To degrade organic pollutants, superoxide radicals ($\cdot\text{O}_2^-$), holes (h^+) and hydroxyl radicals

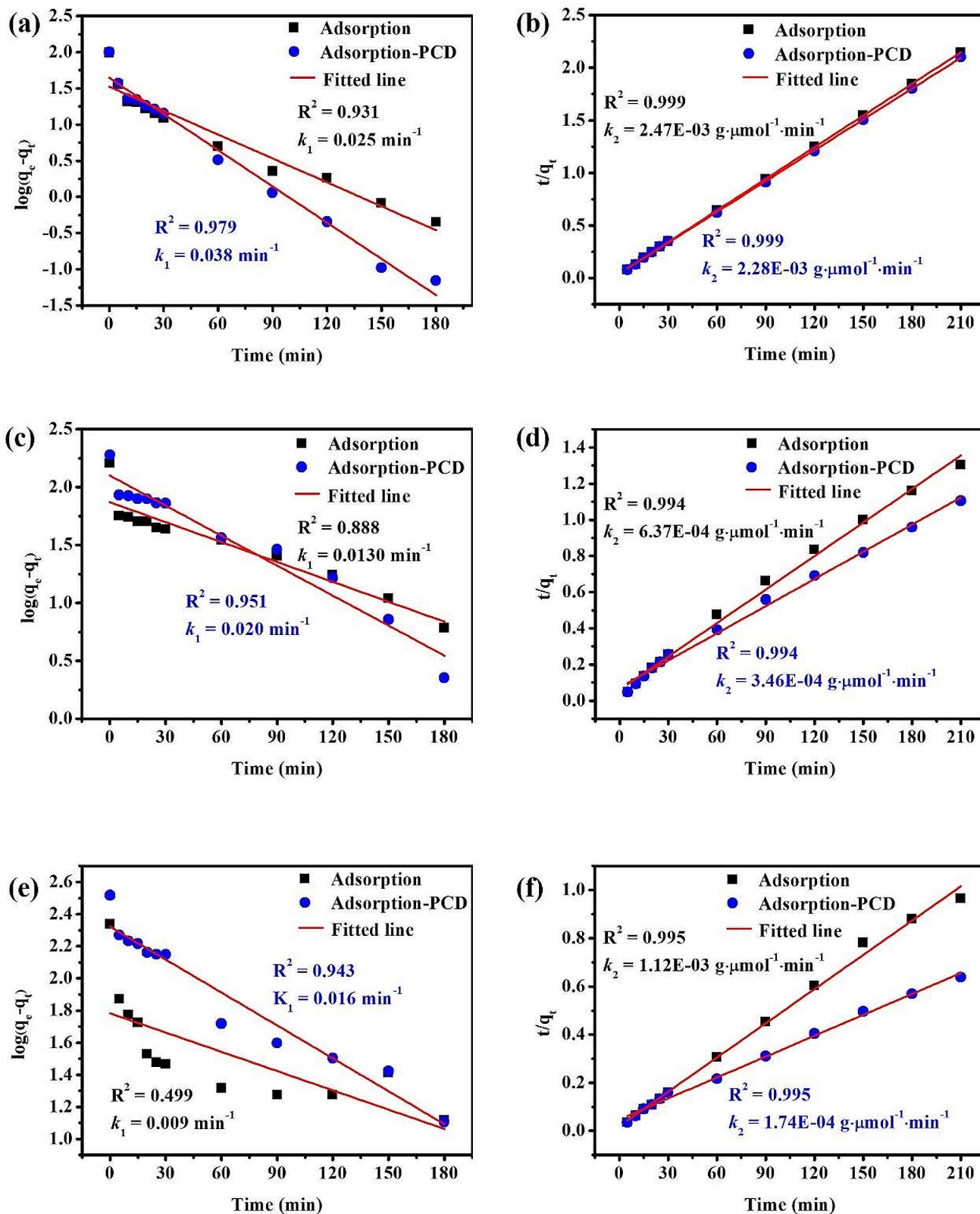
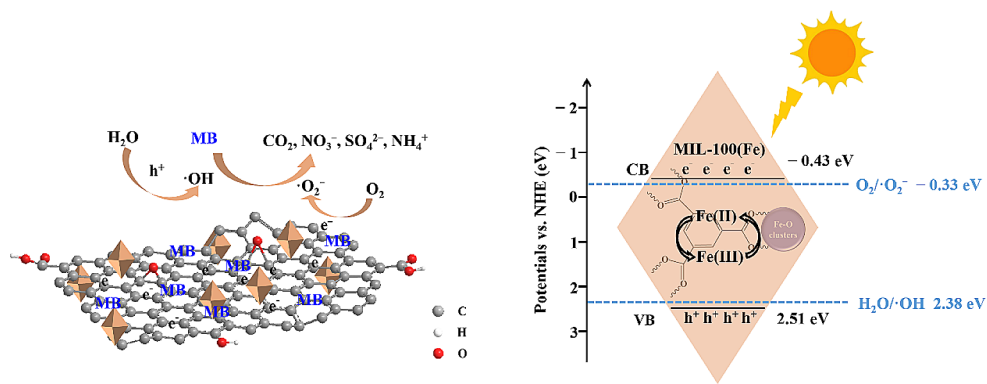


Fig. 10 Pseudo-first order and pseudo-second order kinetic model for MB removal on IM8G at a, b 100, c, d 200, and e, f 400 $\mu\text{mol/L}$

Fig. 11 Mechanism scheme of MB removal over MIL-100(Fe)/GO composite



($\cdot\text{OH}$) with strong oxidizing ability have been regarded as the common active agents. As illustrated in Figure S14, the conduction band (CB) potential of MIL-100(Fe) is extrapolated to be ca. -0.43 eV versus Normal Hydrogen Electrode (NHE), which is negative than $\text{O}_2/\cdot\text{O}_2^-$ potential (-0.33 eV) (Yang et al. 2016). Consequently, molecular oxygen in solution can capture photoinduced electrons (e^-) to form $\cdot\text{O}_2^-$ radicals, which also facilitates the reduction of Fe(III) to Fe(II). The valence band (VB) of MIL-100(Fe) locates at ca. 2.51 eV, which is positive than the $\text{H}_2\text{O}/\cdot\text{OH}$ potential (2.38 eV) (Liu et al. 2018). This render H_2O easily oxidized to $\cdot\text{OH}$ radicals under light irradiation. Importantly, the MB redox potential is less than 1 eV (Zhang et al. 2019), which is significantly lower than the MIL-100(Fe) VB (2.51 eV), indicating the h^+ generated on MIL-100(Fe) VB can oxidize MB. To identify the degradation products, the MB solution after adsorption-PCD reaction were analyzed by ion chromatography. As shown in Table S3, NO_3^- , SO_4^{2-} and NH_4^+ are detected in spent MB solution. Therefore, the MB is degraded into CO_2 , NO_3^- , SO_4^{2-} and NH_4^+ (Chen et al. 2023; Huang et al. 2015). Overall, the $\cdot\text{O}_2^-$, h^+ and $\cdot\text{OH}$ radicals are believed to decompose the adsorbed MB to complete degradation process, as displayed in Fig. 11.

To verify the role of the primary reactive elements in the photocatalytic degradation of MB, tert-butyl alcohol (TBA), ethylene diamine tetraacetic acid (EDTA), and p-benzoquinone (BQ) have been used as scavengers for $\cdot\text{OH}$, h^+ and $\cdot\text{O}_2^-$, respectively (Hejazi et al. 2020). As can be seen in Figure S15, the removal efficiency of MB significantly decrease with the addition of TBA. In contrast, the MB elimination efficiency slightly decrease in the case of EDTA and p-benzoquinone, indicating $\cdot\text{OH}$ is the main active species for MB degradation. Moreover, the electron paramagnetic resonance (EPR) technique is used to evaluate the presence of $\cdot\text{OH}$. The characteristic peaks of the DMPO- $\cdot\text{OH}$ are observed in the EPR spectra of 1M8G under light irradiation (Figure S16), further confirming the important roles of $\cdot\text{OH}$ in MB removal (Li et al. 2019).

The superior adsorption-PCD performance of MIL-100(Fe)/GO hybrid composites is ascribed to the synergetic

effect between MIL-100(Fe) and GO. By introducing GO, the stability of photocatalyst can be improved and several pore structure can be formed at the interface between MIL-100(Fe) and GO layers based on TGA, BET and SEM results. These created pores are beneficial for the mass transfer of reactants and products. The specific surface area and pores size ($30\text{--}50$ nm) of MIL-100(Fe)/GO facilitate the diffusion of MB molecules (1.7 nm \times 0.76 nm) from solution to the surface and pores of MIL-100(Fe)/GO composite. Also, the presence of GO layers suppress the aggregation of MIL-100(Fe) particles resulting in well dispersion, and the formed MIL-100(Fe) restrain the distortion and bundling of GO sheets, which is consistent with literature (Yang et al. 2016). Furthermore, GO with high conductivity provides a highway for electron transfer, and thus retards the recombination of carriers, as confirmed by PL and transient photocurrent results.

4 Conclusions

We have successfully synthesized MIL-100(Fe)/GO via a facile hydrothermal approach, which show superior adsorption capacity and photocatalytic activity to eliminate organic dyes from water. The optimized 1M8G exhibits 95% MB removal (60.8 mg/g) within 210 min under simulated solar light. Moreover, the 1M8G exhibits excellent stability during repeated adsorption-PCD processes for ten cycles. The calculation results of Langmuir model and pseudo-second order kinetic model show that the monolayer chemisorption between MIL-100(Fe)/GO and MB is not only conducive to the effective adsorption of pollutants and the prevention of secondary pollution caused by desorption, but also in favor of the charge transfer in subsequent photocatalytic degradation. The synergistic interaction between MIL-100(Fe) and GO enables effective separation and transfer of photoinduced electrons and holes. The developed MIL-100(Fe)/GO hybrid can be promising candidates for various MOF-based applications including effluent disposal. This work not only provide a new route to remove organic pollutants through

adsorption-photocatalytic degradation method, but also imply the rational design of MOFs based materials.

Supplementary Information The online version contains supplementary material available at <https://doi.org/10.1007/s40789-024-00681-1>.

Acknowledgements This research is supported by the National Natural Science Foundation of China (Grant No.21902001, 22179001) Distinguished Young Research Project of Anhui Higher Education Institution (Grant No.2022AH020007), The University Synergy Innovation Program of Anhui Province (Grant No.GXXT-2023-009) and Higher Education Natural Science Foundation of Anhui Province (Grant No.2023AH050114).

Declarations

Competing interests The authors declare that they have no known competing financial interests or personal relationships that could have appeared to influence the work reported in this paper. The authors declare the following financial interests/personal relationships which may be considered as potential competing interests:

Open Access This article is licensed under a Creative Commons Attribution 4.0 International License, which permits use, sharing, adaptation, distribution and reproduction in any medium or format, as long as you give appropriate credit to the original author(s) and the source, provide a link to the Creative Commons licence, and indicate if changes were made. The images or other third party material in this article are included in the article's Creative Commons licence, unless indicated otherwise in a credit line to the material. If material is not included in the article's Creative Commons licence and your intended use is not permitted by statutory regulation or exceeds the permitted use, you will need to obtain permission directly from the copyright holder. To view a copy of this licence, visit <http://creativecommons.org/licenses/by/4.0/>.


References

- Ahmad M, Chen S, Ye F, Quan X, Afzal S, Yu H, Zhao X (2019) Efficient photo-Fenton activity in mesoporous MIL-100(Fe) decorated with ZnO nanosphere for pollutants degradation. *Appl Catal B* 245:428–438. <https://doi.org/10.1016/j.apcatb.2018.12.057>
- Aslam S, Zeng J, Subhan F, Li M, Lyu F, Li Y, Yan Z (2017) In situ one-step synthesis of Fe₃O₄@MIL-100(Fe) core-shells for adsorption of methylene blue from water. *J Colloid Interf Sci* 505:186–195. <https://doi.org/10.1016/j.jcis.2017.05.090>
- Chen ML, Li SS, Wen L, Xu Z, Li H, Ding L, Cheng YH (2023) Double Z-type ternary composite long-afterglow/graphitic carbon nitride@metal-organic framework for photocatalytic degradation of methylene blue. *J Colloid Interf Sci* 2023(629):409–421. <https://doi.org/10.1016/j.jcis.2022.08.189>
- Du F, Yang D, Kang T, Ren Y, Hu P, Song J, Teng F, Fan H (2022) SiO₂/Ga₂O₃ nanocomposite for highly efficient selective removal of cationic organic pollutant via synergistic electrostatic adsorption and photocatalysis. *Sep Purif Technol* 2022, 295, 121221. <https://doi.org/10.1016/j.seppur.2022.121221>
- Emam HE, Ahmed HB, Gomaa E, Helal MH, Abdelhameed RM (2020) Recyclable photocatalyst composites based on Ag₃VO₄ and Ag₂WO₄@MOF@cotton for effective discoloration of dye in visible light. *Cellulose* 27:7139–7155. <https://doi.org/10.1007/s10570-020-03282-8>
- Ghosh A, Das G (2020) Green synthesis of Sn(II)-BDC MOF: preferential and efficient adsorption of anionic dyes. *Microporous Mesoporous Mater* 297:110039. <https://doi.org/10.1016/j.micromeso.2020.110039>
- Hafizovic J, Björger M, Olsbye U, Dietzel P. D. C., Bordiga S, Prestipino C, Lamberti C, Lillerud K. P (2007) The inconsistency in adsorption properties and powder XRD data of MOF-5 is rationalized by framework interpenetration and the presence of organic and inorganic species in the nanocavities. *J Am Chem Soc* 129:3612–3620. <https://doi.org/10.1021/ja0675447>
- Hailin T, Tirusew A, Ruiping L, Yanfen F, Yingping H (2019) Removal of MC-LR using the stable and efficient MIL-100/MIL-53 (Fe) photocatalyst: The effect of coordinate immobilized layers. *Appl. Catal. B Environ* 254 (2019) 371–379. <https://doi.org/10.1016/j.apcatb.2019.04.086>
- Hameed BH, Din AT, Ahmad AL (2007) Adsorption of methylene blue onto bamboo-based activated carbon: kinetics and equilibrium studies. *J Hazard Mater* 141(3):819–825. <https://doi.org/10.1016/j.jhazmat.2006.07.049>
- Hejazi R, Hjouh AR, Khavar AHC, Hazae Z (2020) Synthesis of novel type visible-light-driven TiO₂@MIL-100 (Fe) microspheres with high photocatalytic performance for removal of organic pollutants. *Journal of Photochemistry and Photobiology A: Chemistry* 2020, 400, 112644. <https://doi.org/10.1016/j.jphotochem.2020.112644>
- Horcajada P, Serre C, Vallet-Regí M, Sebban M, Taulelle F, Férey G (2006) Metal-Organic frameworks as efficient materials for drug delivery. *Angew* 118:6120–6124. <https://doi.org/10.1002/ange.200601878>
- Hu TL, Wang H, Li B, Krishna R, Wu H, Zhou W, Zhao Y, Han Y, Wang X, Zhu W, Yao Z, Xiang S, Chen B (2015) Microporous metal-organic framework with dual functionalities for highly efficient removal of acetylene from ethylene/acetylene mixtures. *Nat. Commun* 6: 7328.10.1038/ncomms8328
- Huang R, Yu Y, Chen Z, Pan D, Li Z, Wu M, Shek C-H, Wu CML, Lai JK (2015) Fe-Loaded Mesoporous MnO₂ Superstructural Requirements for Enhanced Catalysis. *Acs Appl Mater Inter* 2015, 7 (7), 3949–3959. <https://doi.org/10.1021/am505989j>
- Jiang X, Ruan G, Deng H, Gan Z, Zhang W, Du F, Chen Z (2021) Synthesis of amphiphilic and porous copolymers through polymerization of high internal phase carboxylic carbon nanotubes emulsions and application as adsorbents for triazine herbicides analysis. *Chem Eng J* 415:129005. <https://doi.org/10.1016/j.cej.2021.129005>
- Koo HY, Yi DK, Yoo SJ, Kim DY (2004) A snowman-like array of Colloidal dimers for Antireflecting Surfaces. *Adv Mater* 16:274–277. <https://doi.org/10.1002/adma.200305617>
- Li H, Zhou Y, Tu W, Ye J, Zou Z (2015) State-of-the-art progress in Diverse Heterostructured Photocatalysts toward promoting Photocatalytic Performance. *Adv Funct Mater* 25:998–1013. <https://doi.org/10.1002/adfm.201401636>
- Li X, Le Z, Chen X, Li Z, Wang W, Liu X, Wu A, Xu P, Zhang D (2018) Graphene oxide enhanced amine-functionalized titanium metal organic framework for visible-light-driven photocatalytic oxidation of gaseous pollutants. *Appl Catal B* 236:501–508. <https://doi.org/10.1016/j.apcatb.2018.05.052>
- Li H, Xu S, Du J, Tang J, Zhou Q (2019) Cu@Co-MOFs as a novel catalyst for peroxymonosulfate for the efficient removal of methylene blue. *Rsc Adv* 2019, 9 (17), 9410–9420.10.1039/C9RA01143A
- Liu N, Huang W, Zhang X, Tang L, Wang L, Wang Y, Wu M (2018) Ultrathin graphene oxide encapsulated in uniform MIL-88A(Fe) for enhanced visible light-driven photodegradation of RhB. *Appl Catal B* 221:119–128. <https://doi.org/10.1016/j.apcatb.2017.09.020>
- Monika N, Neeraj D, Nitin KS, Ashraf Aly H, Ki-Hyun K, Sandeep K (2018) Metal organic frameworks MIL-100(Fe) as an efficient

- adsorptive material for phosphate management. <https://doi.org/10.1016/j.envres.2018.11.013>
- Nehra M, Dilbaghi, Singhal N, K. N, Hassan H, A. A, Kim K, Kumar S (2019) Metal organic frameworks MIL-100(fe) as an efficient adsorptive material for phosphate management. *Environ Res* 169:229–236. <https://doi.org/10.1016/j.envres.2018.11.013>
- Ou Y, Zhou W, Zhu Z, Ma F, Zhou R, Su F, Zheng L, Ma L, Liang H (2020) Host Differential Sensitization toward Color/Lifetime-Tuned Lanthanide Coordination polymers for Optical Multiplexing. *Angew Chem Int Ed* 59:23810–23816. <https://doi.org/10.1002/anie.202011559>
- Petit C, Bandoz TJ (2011) Synthesis, Characterization, and Ammonia Adsorption Properties of Mesoporous Metal–Organic Framework (MIL(Fe))–Graphite Oxide Composites: Exploring the Limits of Materials Fabrication. *Adv Funct Mater* 2011, 21 (11), 2108–2117. <https://doi.org/10.1002/adfm.201002517>
- Ren J, Li M, Wang X, Li R, Wang H, Yang W (2022) Adsorption behaviors of dyes on a biodegradable gelatin/chitosan/ β -cyclodextrin hydrogel from an aqueous solution. *Colloid Polym Sci* 2022(300 7):785–800. <https://doi.org/10.1007/s00396-022-04988-w>
- Sabboh H, Besson C, Tressol JC, Coudray C, Horcajada M-N, Coxam V, Rémésy C, Demigné C (2006) Organic potassium salts or fibers effects on mineral balance and digestive fermentations in rats adapted to an acidogenic diet. *Eur J Nutr* 2006, 45 (6), 342–348. <https://doi.org/10.1007/s00394-006-0604-0>
- Shuquan Z, Li L, Sangan Z, Zhihua S, Maochun H, Junhua Luo (2015) Hierarchical metal-Organic Framework Nanoflowers for effective CO₂ Transformation Driven by visible light. *J Mater Chem A* 2015(30):15767–15768. <https://doi.org/10.1039/C5TA03322E>
- Sol D, Laca A, Laca A, Diaz M (2020) Approaching the environmental problem of microplastics: Importance of WWTP treatments. *Sci Total Environ* 2020, 740, 140016. <https://doi.org/10.1016/j.scitotenv.2020.140016>
- Soltani D, Azizi B, Rahimi R, Talasaz AH, Rezaeizadeh H, Vasheghani-Farahani A (2022) Mechanism-based targeting of cardiac arrhythmias by phytochemicals and medicinal herbs: a comprehensive review of preclinical and clinical evidence. *Front Cardiovasc Med* 2022(9). <https://doi.org/10.3389/fcvm.2022.990063>
- Tang Y, Xu G, Liu S, Li M, He J, Wen X (2023) Activated carbon microspheres with high surface area for efficient organic contaminants removal. *Colloid Surf A* 2023(669):131479. <https://doi.org/10.1016/j.colsurfa.2023.131479>
- Vargas AMM, Cazetta AL, Kunita MH, Silva TL, Almeida VC (2011) Adsorption of methylene blue on activated carbon produced from flamboyant pods (Delonix regia): study of adsorption isotherms and kinetic models. *Chem Eng J* 168:722–730. <https://doi.org/10.1016/j.cej.2011.01.067>
- Xu WC, Zhong LB, Shao ZD, Dou S, Yu L, Cheng X, Zheng YM (2021) Rational design of pore structures for carbon aerogels to significantly increase adsorption of tetracycline from water using batch and fixed-bed operation. *Environ Sci-Nano* 2021, 8 (11), 3250–3261. <https://doi.org/10.1039/D1EN00459J>
- Yang Z, Xu X, Liang X, Lei C, Wei Y, He P, Lv B, Ma H, Lei Z (2016) (Fe)-Graphene nanocomposites: efficient visible-light photocatalysts for the selective oxidation of alcohols. *Appl Catal B* 2016(198):112–123. <https://doi.org/10.1016/j.apcatb.2016.05.041>
- Zahra S, Naser K, Leila N (2020) Xingmao Ma Elucidating the physiological mechanisms underlying enhanced arsenic hyperaccumulation by glutathione modified superparamagnetic iron oxide nanoparticles in *Isatis cappadocica*. *Ecotoxicol. Environ. Saf.* 2020, 206, 111336. <https://doi.org/10.1016/j.ecoenv.2020.111336>
- Zhang C, Niu Z, Peng S, Ding Y, Zhang L, Guo X, Zhao Y, Yu G (2019) Phenothiazine-based Organic Catholyte for High-Capacity and Long-Life Aqueous Redox Flow batteries. *Adv Mater* 31:1901052. <https://doi.org/10.1002/adma.201901052>
- Zhang L, Wei F, Zhao Q, Chen X, Yao Y (2020) Electrochemical degradation of bromophenol blue on porous PbO₂–ZrO₂ composite electrodes. *Res Chem Intermediat* 2020(2):1389–1404. <https://doi.org/10.1007/s11164-019-04040-7>
- Zhang J, Ma Y, Zhang W, Huang X, Wang X, Huang Y, Zhang P (2022) CuBi₂O₄/calcined ZnAlBi-LDHs heterojunction: Simultaneous removal of Cr(VI) and tetracycline through effective adsorption and photocatalytic redox. *J Clean Prod* 2022, 365, 132810. <https://doi.org/10.1016/j.jclepro.2022.132810>
- Zhou X, Chen Z, Yan D, Lu H (2012) Deposition of Fe–Ni nanoparticles on polyethyleneimine-decorated graphene oxide and application in catalytic dehydrogenation of ammonia borane. *J Mater Chem* 22(27):13506. <https://doi.org/10.1039/c2jm31000g>
- Zhu L, Qu H, Zhang L, Zhou Q (2016) Direct synthesis, characterization and catalytic performance of Al-Fe-SBA-15 materials in selective catalytic reduction of NO with NH₃. *Catal Commun* 73:118–122. <https://doi.org/10.1016/j.catcom.2015.10.023>

Publisher's Note Springer Nature remains neutral with regard to jurisdictional claims in published maps and institutional affiliations.

Authors and Affiliations

Yuxue Wei¹  · Zhiyuan Fu¹ · Yingzi Meng² · Chun Li² · Fu Yin¹ · Xue Wang¹ · Chenghua Zhang¹ · Lisheng Guo¹ · Song Sun¹

✉ Yuxue Wei
weiyuxue@ahu.edu.cn

¹ School of Chemistry and Chemical Engineering, Anhui University, Hefei 230601, Anhui, China

² Anhui Tanxin Technology Co., Ltd, Huaibei 235141, Anhui, China